



Ex situ analysis of high-strength quenched and micro-alloyed steel during austenitising bending process: numerical simulation and experimental investigation

Yao Lu¹ · Haibo Xie¹ · Jun Wang² · Fanghui Jia¹ · Fei Lin¹ · Cunlong Zhou³ · Jianzhong Xu⁴ · Jingtao Han⁵ · Zhengyi Jiang¹

Received: 30 December 2021 / Accepted: 22 April 2022 / Published online: 11 May 2022
© The Author(s) 2022

Abstract

This paper compares the microstructure and mechanical evolution in a high-strength quenched and micro-alloyed steel during the austenitising bending process. Simulation results indicated a new finding that the stress neutral layer (SNL) tends to move to the tension zone during straining. The hardness gradient detected from the centre to compression/tension zones was resulted from comprehensive factors: First of all, the location of SNL revealed a prominent impact on strength. Second, the dislocation accumulation would be responsible for the hardness gradient on the surfaces. In addition, the overall strength decrease during straining was mainly ascribed to integrated effects of dynamic recovery (DRV) and dynamic recrystallisation (DRX). Apart from that, overall smaller martensite packet size and coarser prior austenite grains resulted in the increased hardness value at a lower bending degree. Also, the high consistency between experimental and simulation results is instructive for the practical forming process of railway spring fasteners.

Keywords High-strength quenched and micro-alloyed steel · Austenitising bending · Austenite reconstruction · Numerical simulation · Microstructure · Mechanical property

1 Introduction

High-speed railway develops rapidly and occupies a considerable proportion in the world public transportation. Although the operating speed can reach 350 km/h, a

superior-quality railway system is still one of the goals pursued by public administrators [1]. As a connecting part of rail sleeper and rail steel, the railway fastening system is normally applied to ensure the safety of railway operation, which plays an important role in fixing rail to maintain it with a stable position [2]. However, owing to the cyclic load generated by wheel and rail during the practical operation, the spring clip as one key component of the fastening system would experience failure, compromising the functionality of the railway infrastructure [3–5]. Therefore, the spring clip with high performance is desired to guarantee the safe operation of railway transportation [6].

The 0.55% C Si-Cr steel has been widely concerned with its growing popularity in the development of the new type of spring clips on account of its well-pleasing mechanical properties, e.g. high strength (around 2.5 GPa), toughness (around 130 MPa m^{1/2}), and elongation (around 30%) [2, 7–9], which were ascribed to the dual-phase structure (retained austenite (RA) and bainite ferrite (BF)) [10]. The bainite transformation can be accelerated after the refinement of prior austenite (PA) grains because more nucleation sites would be created for bainite transformation [11, 12].

✉ Zhengyi Jiang
jiang@uow.edu.au

¹ School of Mechanical, Materials, Mechatronics and Biomedical Engineering, University of Wollongong, Wollongong, NSW 2522, Australia

² Welding Engineering and Laser Processing Centre, Cranfield University, Cranfield MK43 0AL, UK

³ Shanxi Provincial Key Laboratory of Metallurgical Device Design Theory and Technology, Taiyuan University of Science and Technology, Taiyuan 030024, People's Republic of China

⁴ Key Laboratory of Rolling and Automation, Northeastern University, Shenyang 110004, People's Republic of China

⁵ School of Materials Science and Engineering, University of Science and Technology Beijing, Beijing 100083, People's Republic of China

As steel with high Si concentration, the carbide precipitation is prohibited greatly due to the low solubility of Si element in cementite during the progress of bainite transformation [13]. It is hard for this steel to be fabricated at a low processing temperature since the transformation of bainite would be greatly suppressed. Thus, in practical fabrication, it is an essential integrant to explore the influence of the high-temperature forming process on the microstructure in terms of optimising the mechanical performance of final products. Nowadays, lots of attention have been concerned with the correlation between microstructures [12, 14], crystallographic features [15], and mechanical properties [16–18] of Mn-Cr-C alloyed steels after hot-working processes. The influence of the hot deformation on 58Mn2SiCr steel [10], 51CrV4 spring steel [19], and high concentration Si steel [20] was discussed in detail previously, as well.

The bending experiments are easy to be achieved at room temperature if the laboratory permits [21], such as the reports regarding pipeline steel [22], high strength steel [23, 24], dual-phase steel [25, 26], and DP 590/780 steel [27, 28]. However, from an application point of view, there is a dearth of investigation on the effects of practical hot forming technology on the final performance of a spring clip, bending at different angles. Theoretically, high-temperature bending is able to bring considerable benefits, for instance, decreasing the spring-back and bending force, increasing the formability, as a result of tailoring and enhancing product performance [29]. To forward the objective of enabling the forming process to be well suited to industrial production, the current work comprehensively investigated the multiple bending conditions on the microstructural and mechanical evolution by combining finite element (FE) simulation with physical experiments. For 0.55% C Si-Cr steel as typical hot-formed material, no research has been concerned before on simulating the practical production. Furthermore, high-temperature microstructural reconstruction was also applied for the first time under this specific forming process. The obtained results will be considered to be a valuable reference for the spring clip manufacturing production.

2 Experiments and simulation

2.1 Process parameters

The testing material in the current work is medium-carbon Si-Cr spring steel (0.55C-1.4Si-0.65Mn-0.65Cr-0.11Ni-0.12Cu-0.012S-0.018P-balanced Fe, in wt.%), which was received from a hot-forged rod. Cuboid samples with a size of $80 \times 10 \times 2$ mm were assembled with a custom-built die (including clamps, sample holders, and punch, as shown in Fig. 1a). The austenitising bending investigation was conducted at 900 °C in a vacuum environment by a Gleeble-3500 thermomechanical simulator (see Fig. 1b). The thermocouples

were spot-welded on the middle area of the specimens to monitor and control the real-time temperature during the bending process. The tantalum foils and graphite were adhered together and spot-welded to the contact areas as lubrication to minimise the influence of bonding and friction during the bending process. The entire bending process was conducted under the lubrication conditions between each contact part. Before bending testing, samples were heated to 900 °C (experimental temperature) with a heating rate of 10 °C/s and held with a duration of 90 s to obtain a homogenised temperature distribution. Whereafter, specimens were bent until the forming distance reached 10, 15, 20, and 25 mm, respectively, with a constant bending speed of 10 mm/min. Watering quenching was used subsequently to retain the high-temperature microstructure for further analysis. The entire bending progress can be conducted with a satisfactory expectation, as illustrated in Fig. 1c.

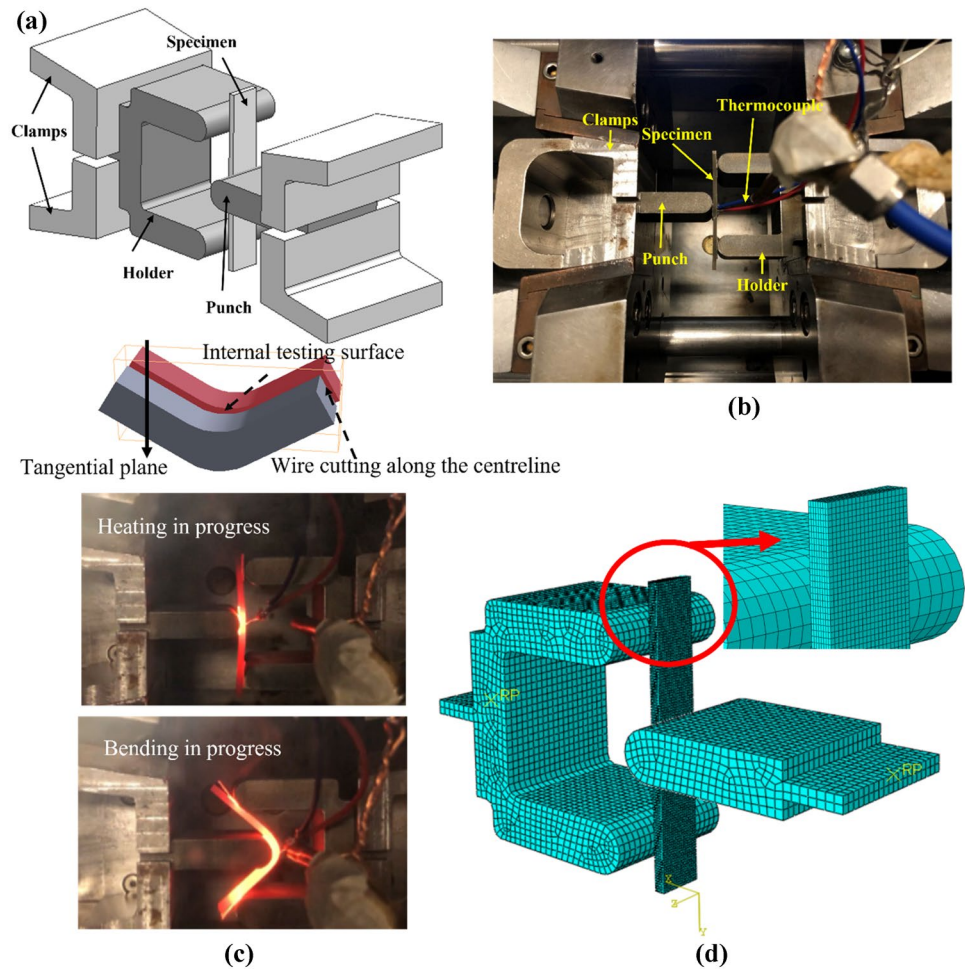
2.2 Material characterisation

To eliminate the variance owing to possible uneven formation at two sides of the experimental specimens, the microstructural and mechanical examinations were focused on the bent area, which was located at the internal testing surface along the geometrical centreline of the specimen (as shown in the inset of Fig. 1a). Sample preparation including hot-mounting, grinding, and polishing was conducted based on the standard metallographic technique given in our previous study [1]. Electron backscattered diffraction (EBSD) experiments were carried out on a JEOL JSM-7001F field emission gun scanning electron microscope for the microstructural observation with a scanning area of 200×90 μm and a step size of 0.18 μm ; then, the obtained data was post-processed by HKL Channel 5 software. The parent grain reconstruction was achieved by the MTEX toolbox, which enables the traditional phase transformation, prior austenite grain, and variant investigation to extend to all crystal symmetry combinations [30].

2.3 Finite element (FE) modelling

The ABAQUS/Standard software was used to conduct the simulation investigation. To well simulate the whole process, all the simulated parameters were consistent with the experimental ones. The model was built based on the relevant mechanical properties from our previous studies [1, 13]. The yield and tensile stresses were determined to be 84.2 and 138.6 MPa, respectively. The Young's modulus was set to be 210 GPa. Besides, the Poisson's ratio in this study was selected to be 0.33. In this modelling, holder and clamp were defined as discrete rigid bodies with the element type of R3D4, and the blank was built as deformable solid model with the element type of C3D8R. The simplified assembly

Fig. 1 **a** Schematic of the custom-built die with the bent sample; **b** Gleeble 3500 thermo-mechanical simulator assembled with the experimental sample; **c** state monitoring of the bending progress; **d** mesh model



mesh model was displayed in Fig. 1d. Besides, the displacement was classified by four values (10, 15, 20, and 25 mm). Due to the lubrication condition, the coefficient of friction was chosen to be 0.1 between all the contact areas [31]. Initially, there was no constraint for blank, while the holder and clamp were constrained in all directions. The punch was defined with one freedom along the bending direction. The model of blank meshed with the element size of 0.5 mm, and 1.5 mm was defined for all the other rigid bodies.

3 Results

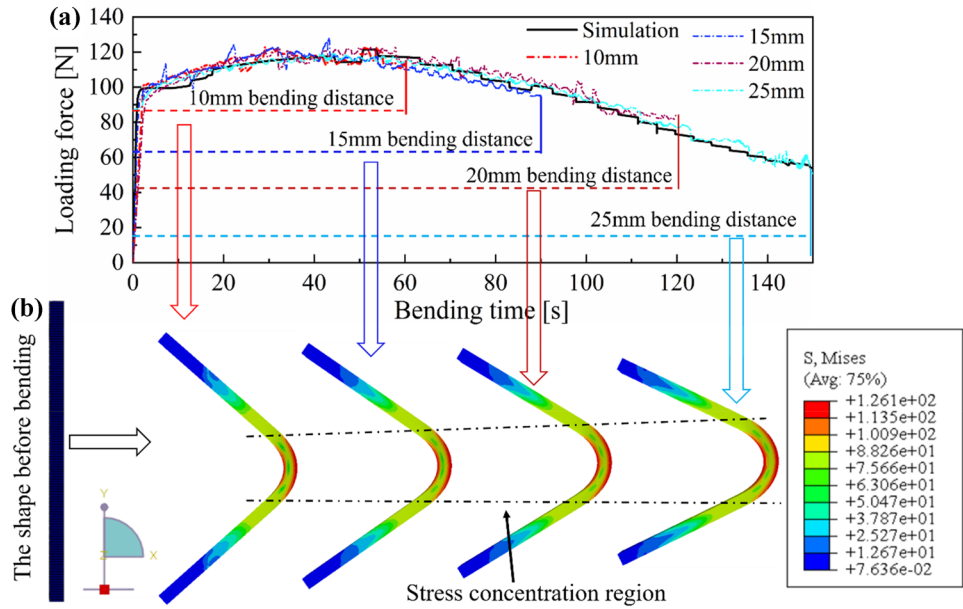
3.1 Verification of FE modelling

To obtain the stress distribution of the experimental steel during the whole forming progress, numerical simulation was employed to simulate the austenitising bending process (see Fig. 2). In industrial production, it is necessary to explore the influence of working conditions on the macroscopic properties, such as loading force, which was considered to be a valuable reference for practical manufacturing

[32]. Figure 2a displays the force evolution with different bending distances. Notably, the reliability and accuracy of the simulation can be validated from the good agreement of experimental and simulation results. At the early stage of bending progress, all curves presented a short region of rapid work hardening, followed by a decreased rate of force increment with distance, which was attributed to the main dynamic recovery (DRV) behaviour based on the principal mechanism [33]. In addition, the force curves showed peak values when the bending time reached around 50 s due to the neutralisation of work hardening and dynamic softening. Whereafter, the major dynamic softening process led to a continuous decrease in force because of the dislocation rearrangement and annihilation [13]. Obvious decreased forming force can be observed under a larger strain condition, implying the dominant softening mechanism caused by the dynamic recrystallisation (DRX) [1].

The developed stages in the simulation process being carried out are represented in Fig. 2b. Notably, the equivalent stress contour exhibits that the stress magnitude had an increasing trend from centre to surface throughout the thickness of the bent plates. Furthermore, the concentration

Fig. 2 a Comparison of experiments with simulation in the relationship between forming force and loading distance; **b** equivalent stress distribution under different bending degrees



fields of equivalent stress increased, as well. Considering the goodness of fit between experiments and simulation, it unfolds actual physical stress evolution and concentration, which would provide a reference for the following microstructural and mechanical analysis.

3.2 Micro-hardness transition and bending strain calculation

Miro-hardness transition across the bent region during the austenitising bending process is exhibited in Fig. 3.

Figure 3a displays the hardness variation after deformation as a function of the distance throughout the thickness of bent plates. Apparently, a relatively homogeneous distribution can be observed when the bending distance moved to 10 and 15 mm. However, with a further bending deformation, the hardness distribution became inhomogeneous and such inhomogeneity will be aggravated as increased bending distance from 20 to 25 mm. Besides, the overall tendency represents that hardness always decreased from both surface edges towards central regions, and the maximum value was located at the outer surface of each bent specimen. The accumulated

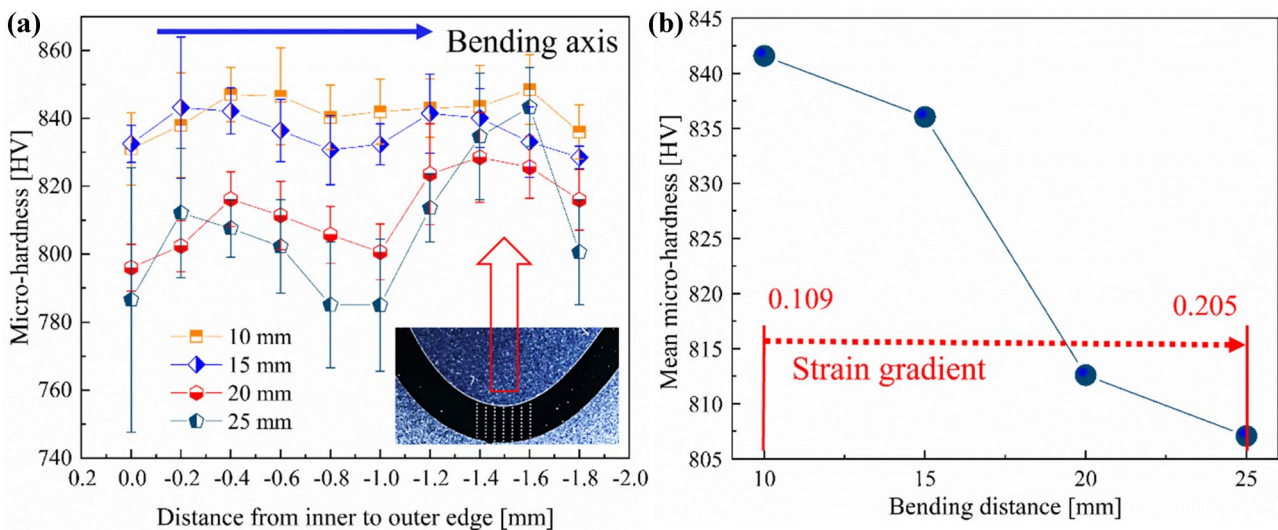


Fig. 3 a The hardness transition along the bending axis at different moving distances; **b** comparison of mean hardness under various conditions. The development of strain gradient owing to austenitising bending was plotted

dislocation may be responsible for the improved hardness on both surfaces. Furthermore, a relatively smaller hardness value measured on two sides was an interesting finding as well, which may be attributed to the oxidation or decarburisation. This is because the water quenching process is followed by vacuum-unloading after deformation, the air would be brought in so that the oxidation occurs on the surface of the material.

Mandal et al. [22] and Sohn et al. [34] have reported the calculation method of strain $\epsilon(d)$ on any plane due to the bending process at a distance by the equation shown below:

$$\epsilon(d) = 2d/(R - t) \tag{1}$$

where d is the distance from the centre of the plate thickness and R and t indicate the outer bent-diameter and plate thickness, respectively. The strain is negative in compression zone, i.e. from neutral axis to inner edge and positive in tension zone, i.e. from neutral axis to outer edge. The

strain gradient increased from 0.109 to 0.205 at the tension and compression zones of the bent specimens where the bending distance was determined in the range of 10–25 mm (see Fig. 3b). The variation of hardness and microstructure cannot be avoided completely due to the bending strain result of the austenitising bending; thus, the mean hardness decreased from 842 to 807 HV, which illustrates the gradient in microstructure throughout plate thickness is large in this study. Normally, a dominant softening process resulted from DRX is the main factor that leads to decreased hardness with the increase of bending strain. Except for that, the hardness decreased during strain could also be attributed to the resultant growth of martensitic microstructure. This is because, under the uniform bending speed, a larger deformation degree requires more high-temperature duration, which is beneficial for the growth of quenching microstructure. The detailed microstructure evolution will be further clarified in the following sections.

Fig. 4 Schematic testing surface; bending axis; inverse pole figure (IPF) figures of the bent plates under different bending distances: **a–b** 10 mm, **c–d** 15 mm, **e–f** 20 mm, and **g–h** 25 mm. CE, central area; OE, outer edge. Note, the crystallographic orientation-colour relation map corresponding to the colour-coded stereographic triangle IPF

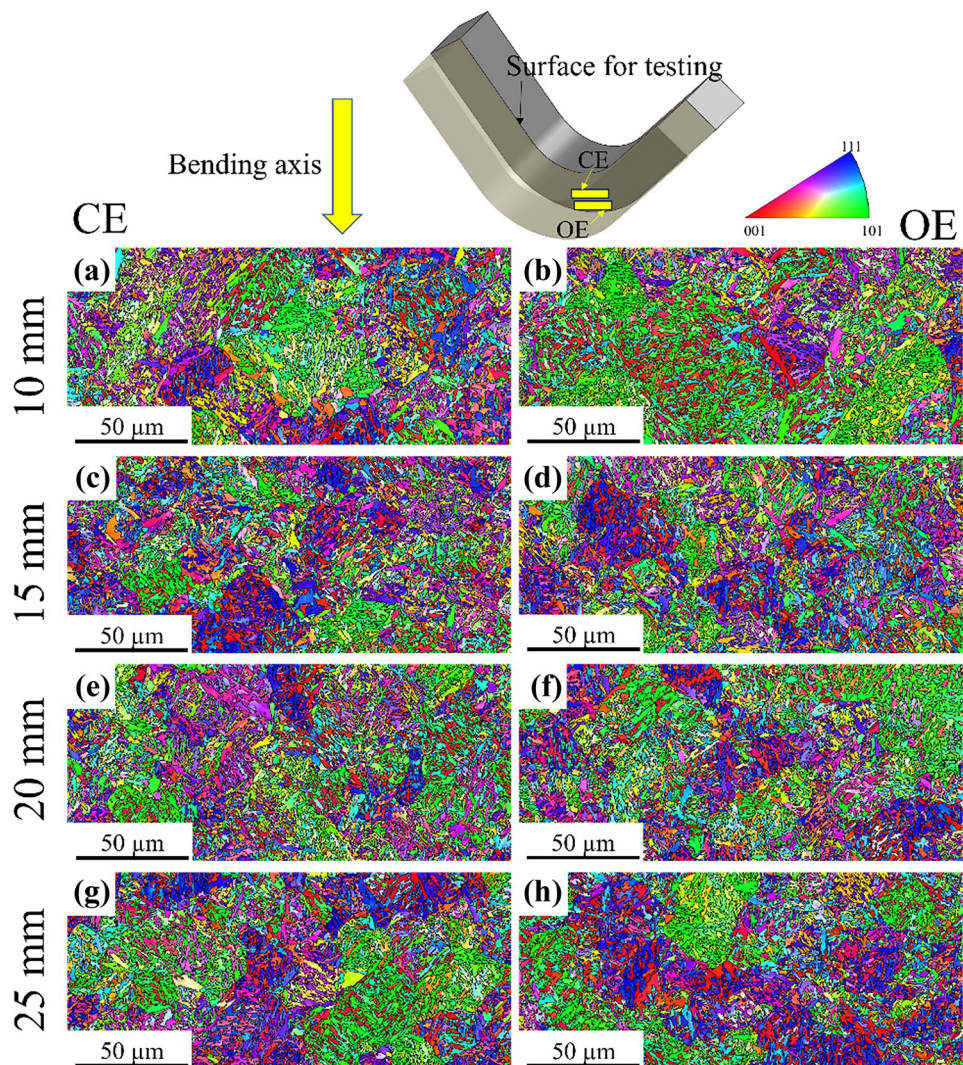
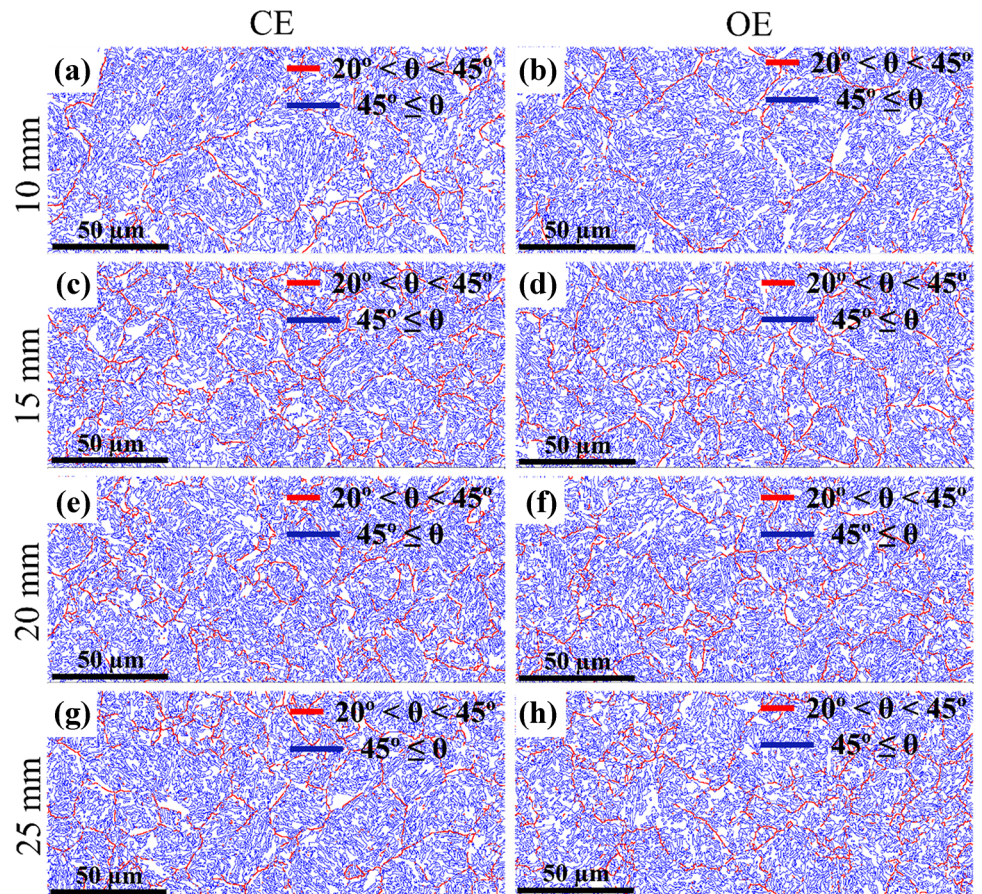


Fig. 5 Grain boundary (GB) figures of the bent plates under different bending distances: **a–b** 10 mm, **c–d** 15 mm, **e–f** 20 mm, and **g–h** 25 mm. CE, central area; OE, outer edge



3.3 Crystallographic features

In comparison to austenitic modal steels, the austenitic substructures of the experimental steel are not so prominent after hot deformation owing to phase transformation, whereas the crystallographic features were still greatly influenced by various metallurgical events during the austenitising bending process [1]. In response to the evident variations of microhardness between mid-thickness and inner/outer surfaces with different bending conditions, EBSD mappings were performed focusing on two specific regions (CE, central area: nearby geometric centreline; OE, outer edge: located in tension zone) throughout each sample thickness (see Fig. 4).

Lath martensite (LM) normally occurs in steels with a carbon content of no more than 0.6 wt.% [35]. Besides, the theoretical Kurdjumov–Sachs (K-S) relationship of which is applied to reflect orientation correlation between austenite and LM are well known in carbon steels [36]. From inverse pole figure (IPF) figures obtained from the current study (as shown in Fig. 4a–h), it is apparent that the orientation domains were evenly distributed regardless of austenite condition. This is because the phases generated during the entire bending process are thought to abide by K-S rules, which have 24 variants. Certain combinations of variants possibly

have ten misorientation angles, i.e. 10.53°, 14.88°, 20.61°, 21.06°, 47.11°, 49.47°, 50.51°, 51.73°, 57.21°, and 60.00° [35]. The minimum misorientation angle was selected to be 10.53° in IPF figures, aiming to distinctly outline the grain boundary. In addition, the IPF graphs show near no relevance between bending axis and grain distribution, which could also be verified by grain boundary (GB) figures exhibited in Fig. 5, where misorientation angles in the range of 20–45° were plotted by bright red and the area with blue was an indication of misorientation angles over 45°.

Since the PA was reported to be equipped with stochastic misorientation boundaries [33], special division of misorientation angles given above was a new discovery for this investigation, which is only acceptable in the experiment steel with the austenitising forming process. In this study, the bright red lines may suggest the distribution of DRX grains. Although it shows little deviation in different regions of a bent plate, the distribution of red lines increased significantly with the increase of bending distance. This illustrates the degree of DRX increases as the bending strain accumulated, which verifies the decreased hardness values mentioned above. Furthermore, the bigger area without red lines was the indication of non-recrystallised austenite grains and compressed/grown austenite matrix [33].

By comparing the grain boundary characteristic distributions of samples bent at different distances, the misorientation angle distributions are plotted in Fig. 6a–d, presenting similar distribution patterns in all conditions. To consume the transformation strain during hot deformation process, previous studies have reported the low-angle grain boundaries (LAGBs) in the range of 2 to 5° was an indication of transformation dislocation [37, 38]. A larger proportion of LAGBs normally indicates a higher dislocation density. It is obvious from the insert bar graphs in Fig. 6a–d that LAGBs occupy a higher proportion at OE in comparison to those at CE of each bent plate, implying the dislocation was accumulated from centre to surfaces throughout the plate thickness. These results further demonstrate the difference in hardness transition between CE and OE. In addition, as shown in Fig. 6e, the overall LAGBs developing trend under different bending distances experienced an increase from 10 to 15 mm. However, a decreasing tendency was obtained in 20 mm, followed by another increase when the plate moved to 25 mm. This would be ascribed to multiple factors [39]. First of all, the continuous accumulation of dislocation is beneficial for the new formed DRX nucleation due to the unstable thermodynamical process, indicating that the DRX and dislocation can neutralise each other during straining [33]. DRX lied in a dominant status with the reduction of high-temperature DRV before 20 mm. Besides, it has been proposed by Sun et al. [39] that the high-angle grain boundaries (HAGBs) represent DRX phenomenon to some extent.

It can be observed that the degree of DRX in OE was greater than that in CE based on the calculation of HAGBs of each plate (see Fig. 6e). Owing to the continuous increasing proportion of HAGBs, it is conjectural that DRX completed after 20 mm but before 25 mm. The possible clarification is the accumulated dislocation was consumed by DRX before 20 mm, while the dislocation density increased again after 20 mm owing to complete DRX at this condition. Thus, the DRV occupied the major status after the 20 mm bending process as the result of the second rise in LAGBs.

3.4 High-temperature microstructure

In terms of the microstructures after hot deformation process on the carbon steels, a certain amount of researches have been reported before [1, 13, 40–44]. However, no relevant research has been concerned with the high-temperature microstructures of the experimental steel after a specific hot-working process. In the current work, reconstructed EBSD data with PA grain boundaries was successfully integrated into crystallographic toolbox MTEX from completed or partially transformed microstructures (see Fig. 7) when applying the technique proposed by Frank et al. [30]. This enables to list the child α -grains belonging to a specific parent γ -grain and is crucial for analysing subsequent variants. Note that the PA structures exhibit a relatively larger grain size at 10-mm bending distance on both CE and OE, along with the occurrence of tiny DRX grains nucleated at the parent grain

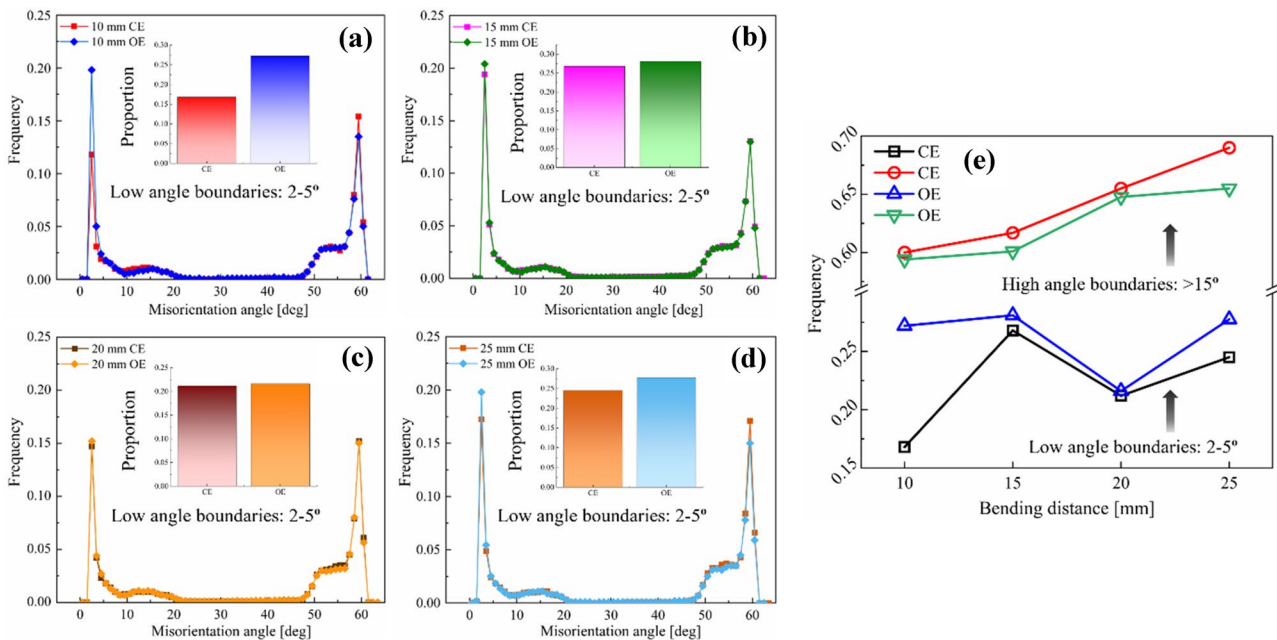
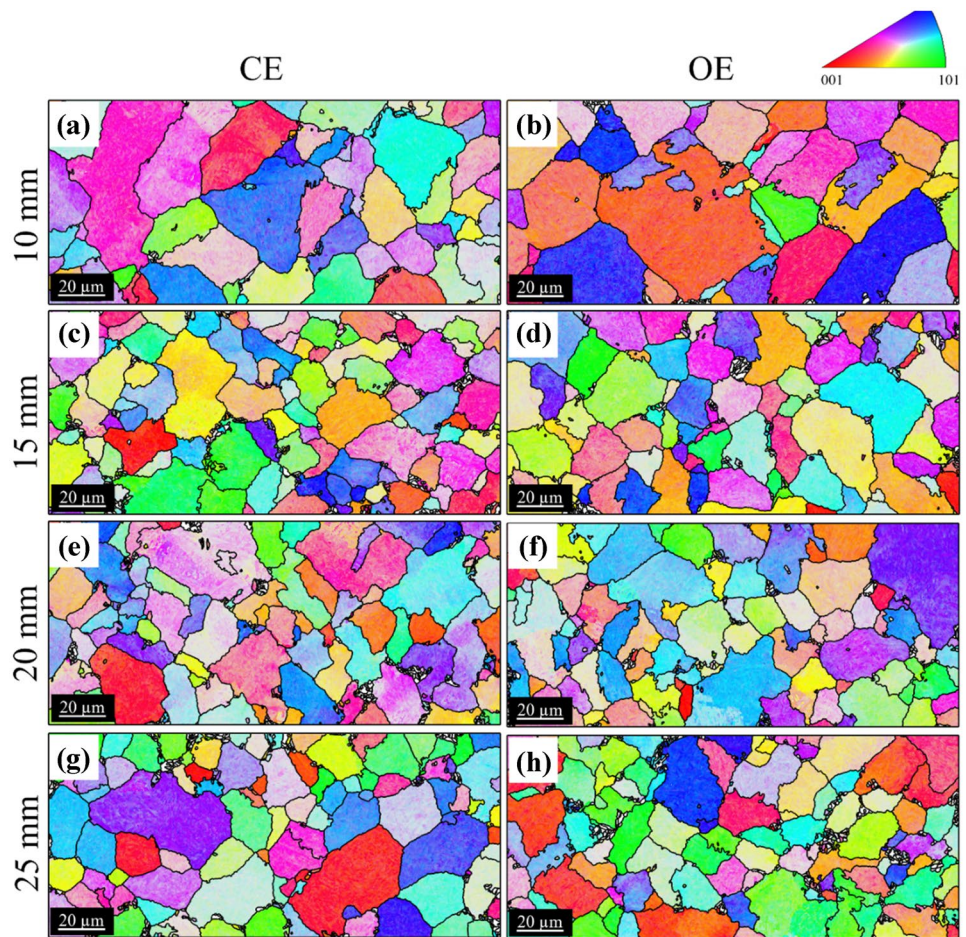


Fig. 6 Grain boundary characteristic distributions of CE and OE obtained from the bent plates under different bending distances: **a** 10 mm, **b** 15 mm, **c** 20 mm, and **d** 25 mm; **e** Comparison of low- and high-angle boundaries in each bending condition. CE, central area; OE, outer edge

Fig. 7 Reconstruction of parent austenite grains for the specimens bent at **a–b** 10 mm, **c–d** 15 mm, **e–f** 20 mm, and **g–h** 25 mm. CE, central area; OE, outer edge



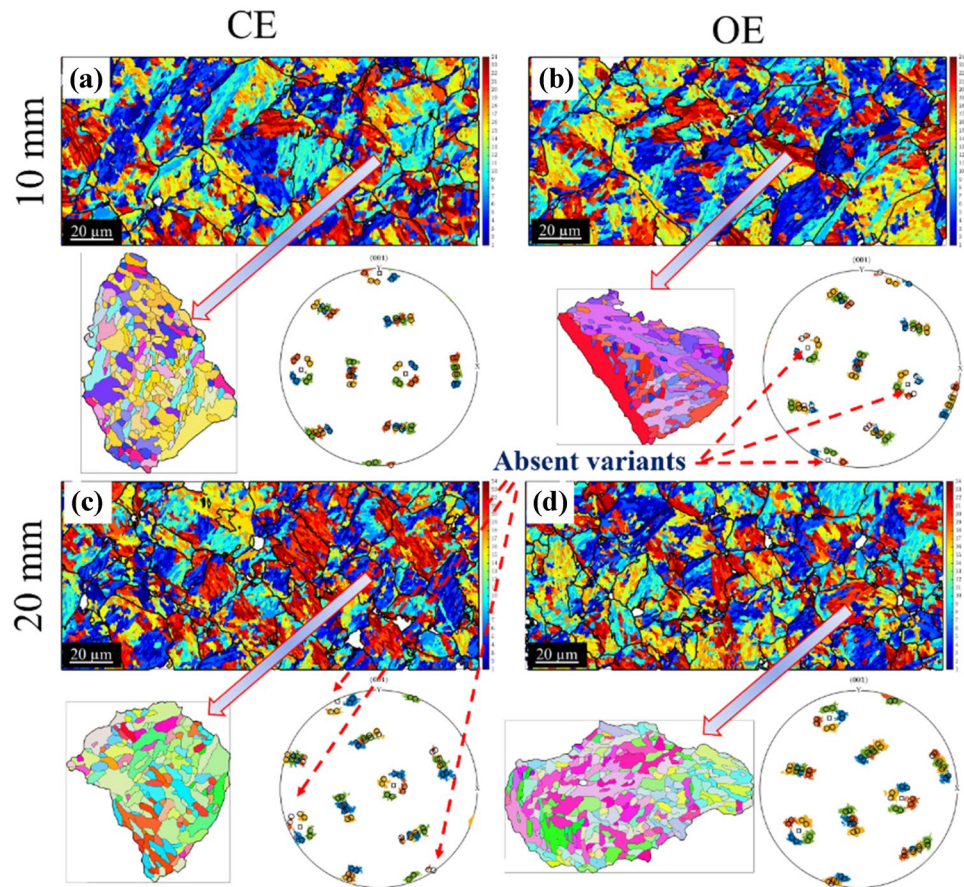
boundaries (Fig. 7a–b). The predicted PA grain size was subsequently refined during straining (Fig. 7c–f) as severer bending strain prolonged the high-temperature interval. This effect hinders the extent of grain growth when the amount of newly nucleated DRX grains was increased. Although there was insignificant difference can be detected from Fig. 7c–f, it is assumable that the larger bending strain allows more parent grain nucleation sites to get active, leading to a higher grain density as a result of smaller parent grain size [45]. The appearance of grown grains on both tested areas at the 25-mm bending distance (Figs. 7g–h) does not seem to follow the logic of the abovementioned PA growth and nucleation mechanism; it may indicate the possibility of fully DRX under this bending condition.

3.5 Martensite variants

As mentioned in Sect. 3.3, since LM structure is usually formed in steels with a carbon content of less than 0.6 wt.% [35], the investigated steel is expected to obtain a K-S relationship between martensite (α') and austenite (γ), which can be described as $(111)\gamma // (011)\alpha'$, $[\bar{1}01]\gamma // [\bar{1}\bar{1}1]\alpha'$. In a given

packet and the corresponding γ matrix, there are 6 K-S orientation relationship variants, named V1 to V6. It has been reported by Morito et al. [36] that the V1 and V2 show a twin orientation relationship when V1 is used as the base variant. The V1 and V3 show a relationship of $[011]/60^\circ$, and the same orientation can be observed between V1 and V5. Besides, V1 and V6 exhibit an orientation of $[011]/49.5^\circ$. Each austenite grain has four different $(111)\gamma$ orientations. Given this the relationship exists, the cubic structure is equipped with 24 variants (represented as V1–V24), which all transform from single austenite [35, 36, 46, 47]. Figure 8 illustrates the evolution of martensite variants in the specific austenite grains of the specimens bent at 10 mm (dominant DRV) and 20 mm (dominant DRX). Apparently, a certain number of martensite variants are distributed within different austenite grains regardless of the bending process. Nevertheless, more absent variants were indicated in Fig. 8b and c in comparison to Fig. 8a and c, respectively. This may suggest the larger parent grain size provides enough nucleation space for the martensite structure. Normally, the absent variant was thought to be the natural phenomenon due to the lack of transformation space [48], depending on the PA grain size [47].

Fig. 8 Variants of martensitic structure and the corresponding pole figures in selected prior austenite grains of the specimens bent at **a–b** 10 mm; **c–d** 20 mm. CE, central area; OE, outer edge



4 Discussion

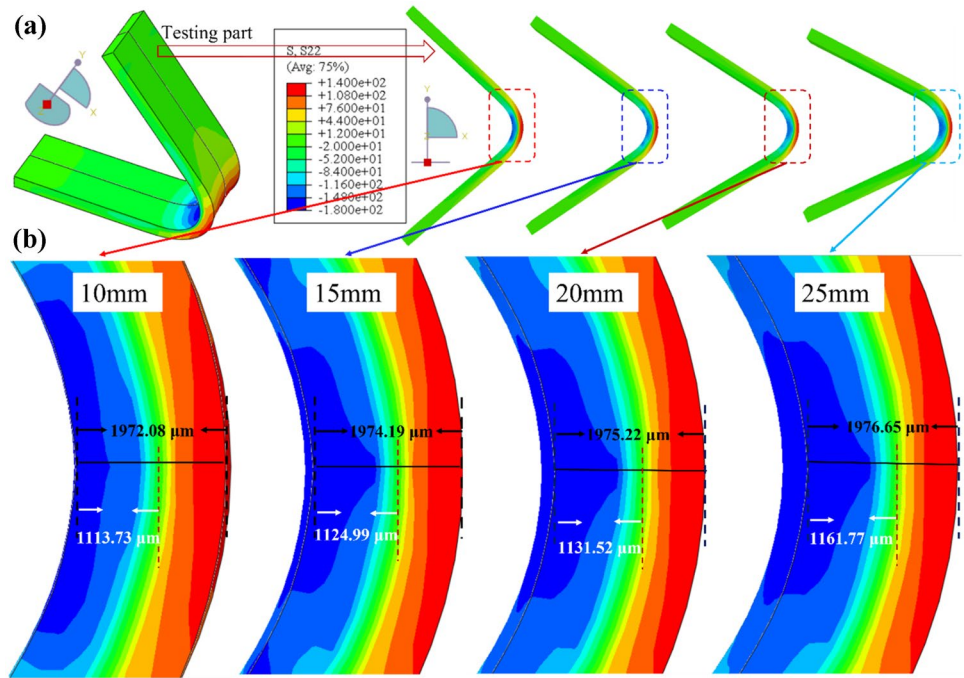
Understandably, the hardness would exhibit a transition with different bending distances. Differences in the hardness value will also show up between middle areas and tension/compression zones. Actually, a combination of factors would be responsible for this, which will be discussed in detail in the following sections.

4.1 Role of stress neutral layer in deformation

The developed distributions of transverse stress (S_{22}) are shown in Fig. 9a. To get consistent and accurate results, the predicted location of the testing surface is carried out inside the part, which is separated by the centre line along the width. Moreover, Fig. 9b shows the magnified bent regions at different bending degrees. Through the simulation prediction, the plate thickness (PL) revealed a slight decrease at all conditions since the flowability of metallic material would be enhanced at a high-temperature forming process [49]. However, with the increase of bending distance, the PL increased a bit (see Fig. 10a) due to a larger stress and stress concentration area that may affect the sample to be squeezed in this region.

Furthermore, the stress neutral layer (SNL) is defined as the critical layer connecting compression and tension zones at a certain bent degree, so that the surface at the extrados is thought to be the tension zone, whereas that at the inner edges is called the compression zone [50]. Therefore, it is not difficult to conclude that the minimum hardness occurs at the position of the geometric centreline and increases gradually from the centre to the edge due to the presence of SNL. As for this simulation, neutral layer thickness (NLT) was defined to be the distance between the inner edge and the neutral stress layer, which shows a rising tendency from 1113.73 to 1161.77 μm . It has been proposed that SNL tends to move towards the inner surface during the ambient bending process [51], while the movement of the SNL during the high-temperature bending process is rarely mentioned. In the current work, an interesting finding is proposed that the movement of SNL transferred to the outer surface through the thickness of bent plates with the increase of moving distance based on the ratio of NLT to PT as displayed in Fig. 10b, implying opposite results to that of room temperature. Moreover, reports provided by Li et al. [51] mentioned that the SNL is dependent on some integrated factors such as the deformation mechanism, type of alloy, and plastic strain accumulation. In practical manufacturing process, SNL as

Fig. 9 **a** Transverse stress (S22) distribution at different bending degrees; **b** High-magnification observation of plate thickness and stress neutral layer location



a vital indicator vastly influences the process parameters, straightness precision, and roller design of steel bars [52].

4.2 Dislocation pile-up for GND density in deformation

Kernel average misorientation (KAM) maps are normally applied to describe the orientation gradients with the specific range in individual grains [40]. In this study, the selection

of boundaries was determined within 5° and the 7×7 filter KAM maps were appropriate here, as displayed in Fig. 11. For the plates bent at different conditions, some typical areas were picked out due to relatively higher local strain (labelled by red ellipses), as shown in Fig. 11a–c and e). In comparison to other deformed areas, evidence of non-recrystallised austenite grains can be captured in these regions before phase transformation, further confirming the occurrence of regional DRX. Although the generated phase would inherit plastic strain correlative with deformed austenite according to the

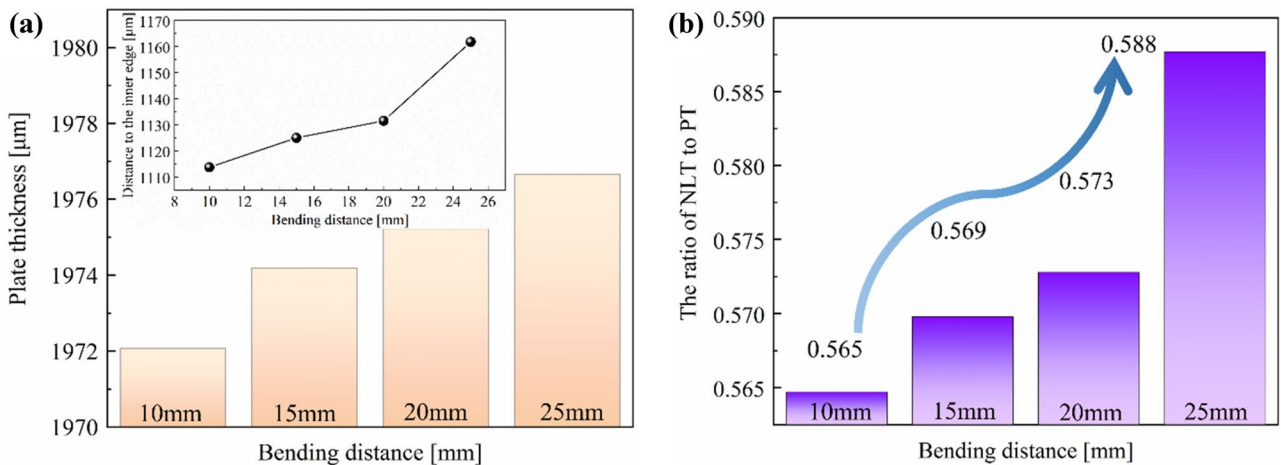


Fig. 10 **a** Comparison of plate thickness and neutral layer thickness at different bending distances; **b** the ratio of neutral layer thickness to plate thickness

shear mechanism, the majority of the plastic strain would be offset by DRX. Besides, Fig. 11 also shows the brighter colour indicated on OE in comparison with CE of each bent plate and on the plate with a larger bending distance as the dislocation pile-up occurred in this case, as well.

Local misorientation comparisons shown in Fig. 11 reveals that the geometrically necessary dislocations (GNDs) would be significantly affected due to strain portioning and heterogeneity in microstructure [13]. Although the KAM characteristic is unable to directly illustrate the dislocation, it has been proved to be a representative result for dislocation observation in comparison with TEM [53]. The plastic deformation leads to the local misorientation, resulting from GNDs correlative with curvature of the crystal lattice and influence of elastic strain. The lattice curvature was considered to be the unique factor related to the presence of GNDs due to the primary effects of lattice rotation than those of elastic field [54]. The local crystal orientation in different bent regions was measured at the above selected bending strains to further discuss the GNDs. In this study, it is acceptable to calculate the local misorientation when defining the limit of random misorientation as 2°. The local misorientation of each central point was then ruled by the 8 neighbour points [13, 55]:

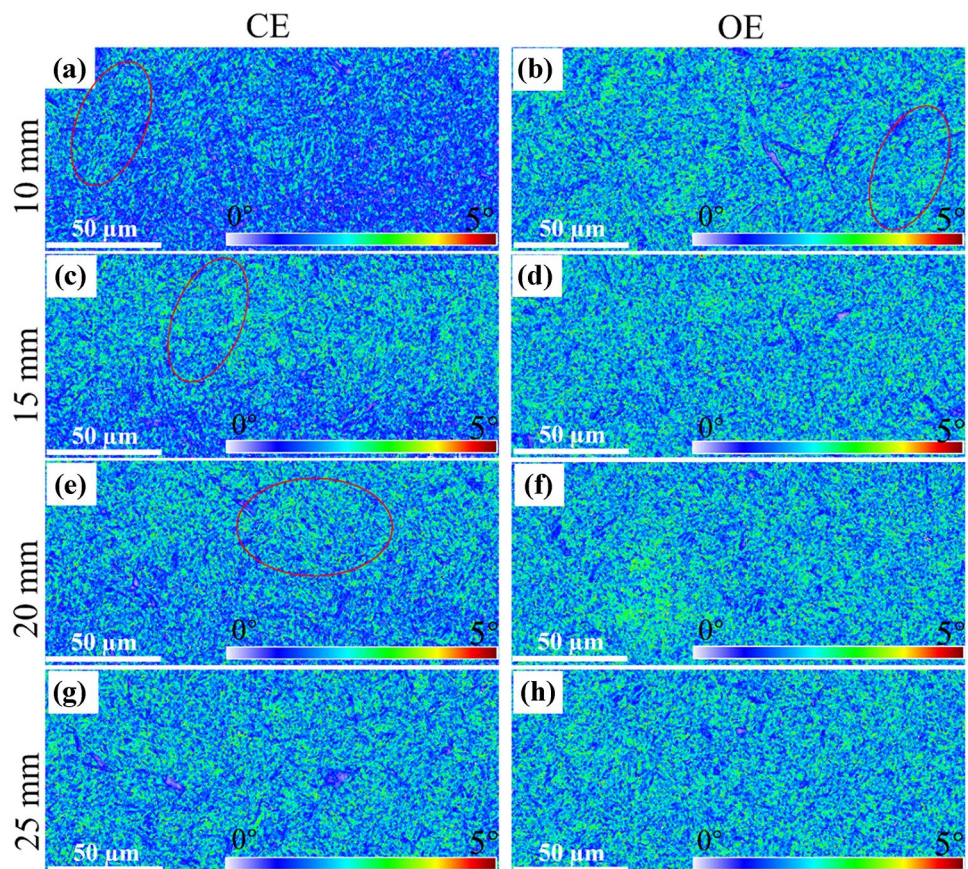
$$\theta_{local} = \frac{\sum_{n=1}^8 \theta_n \cdot I_{(\theta_n < \varnothing)}}{\sum_{n=1}^8 I_{(\theta_n < \varnothing)}} \quad (2)$$

where θ_n represents the misorientation between this central point and its neighbour point n , \varnothing is the misorientation threshold (2°), and the indicator function is defined as $I_{(\theta_n < \varnothing)}$. The simple method from strain gradient theory was applied to extrapolate GNDs [56]:

$$\rho^{GND} = \frac{2\theta}{ub} \quad (3)$$

where θ refers to the local misorientation, u represents the mapping unit length (step size), and b is the Burger’s vector (BCC: 0.248 nm). The obtained histogram GND distribution maps are identified in Fig. 12 for all the specimens under their corresponding bending distances. Apparently, the overall level of GND density was higher on OE than that on CE (see Fig. 12a–d), which was our anticipated result due to the inhomogeneity of polycrystalline materials during deformation [57, 58]. This is another element for the higher hardness on the surfaces. The increased GND density is mainly caused by the increasing plastic strain [56] which is also compatible with the fact that a higher local strain is needed to accommodate bigger transformation plastic strain

Fig. 11 Kernel average misorientation (KAM) maps of CE and OE obtained from the bent plates under different bending distances: **a–b** 10 mm; **d–e** 15 mm; **g–h** 20 mm; **j–k** 25 mm. CE, central area; OE, outer edge



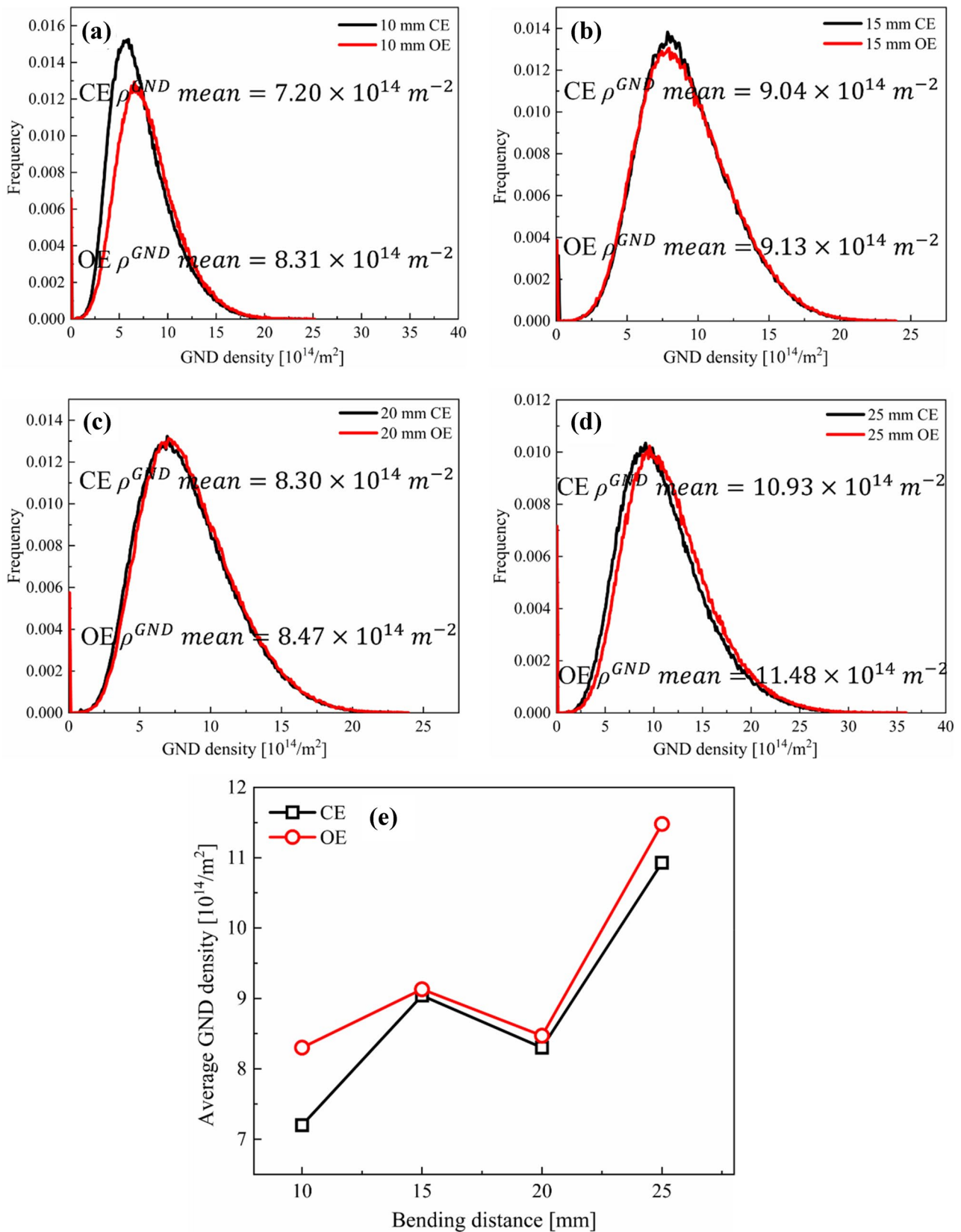


Fig. 12 GND density distribution of specimens bent at **a** 10 mm, **b** 15 mm, **c** 20 mm, and **d** 25 mm; **e** comparison of mean GND density under each bending condition. CE, central area; OE, outer edge

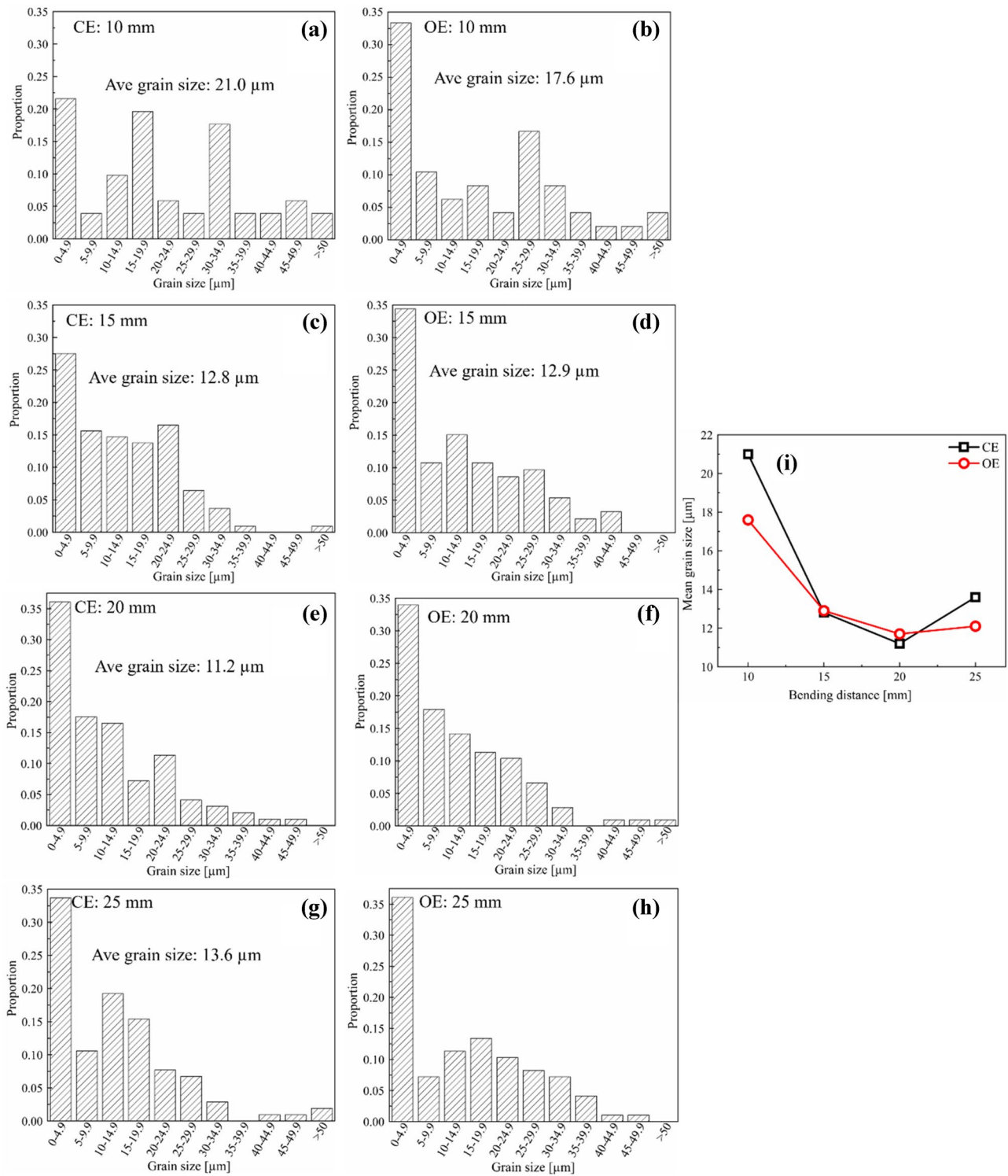


Fig. 13 Distribution of parent austenite grains for the specimens bent at 10 mm (a) and (b); 15 mm (c) and (d); 20 mm (e) and (f); 25 mm (g) and (h); i comparison of mean parent grain size of each bending condition. CE, central area; OE, outer edge

[40]. Higher plastic strain is thought to be inherited for the plate bent at 25 mm (Fig. 12d) due to dominant DRV in this case after the completed DRX, which can be verified

from the mean value GND density ($10.93 \times 10^{14} \text{ m}^{-2}$ and $11.48 \times 10^{14} \text{ m}^{-2}$ on CE and OE, respectively). It is also noted from Fig. 12e that the GND density for each bent

Fig. 14 Comparison of the packet size of the specimens bent at **a–b** 10 mm; **c–d** 15 mm; **e–f** 20 mm; **g–h** 25 mm. CE, central area; OE, outer edge

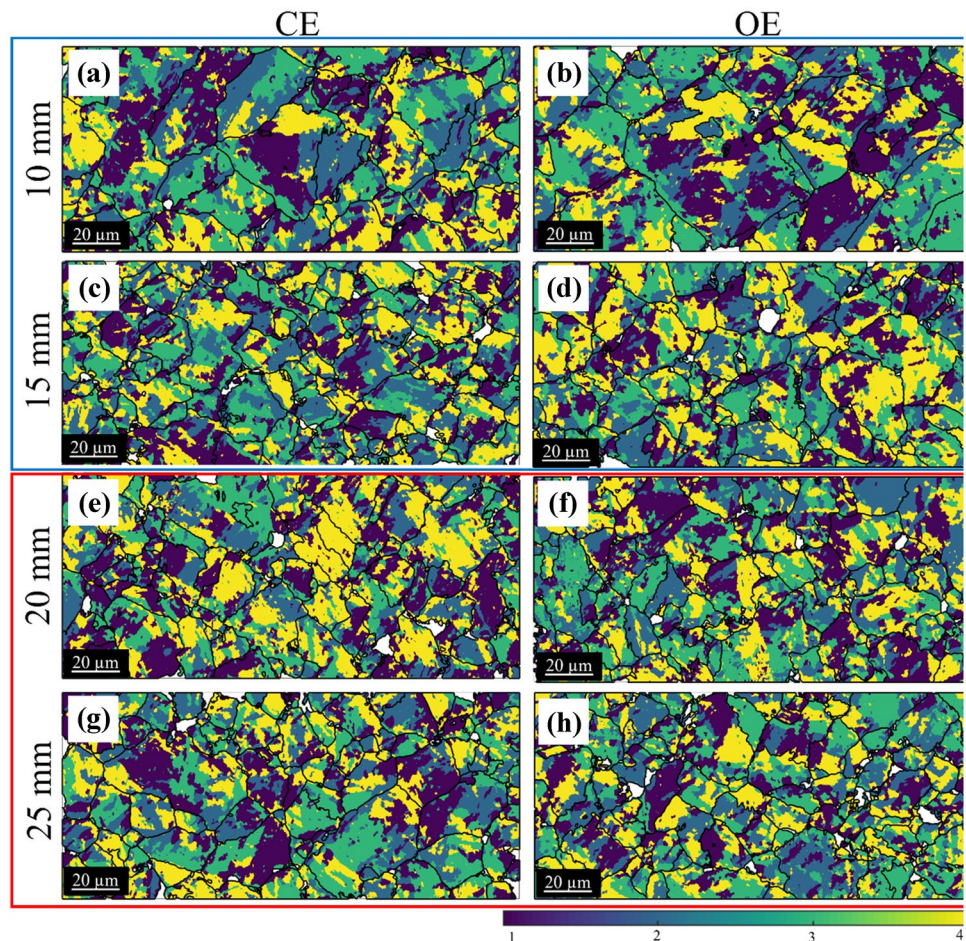


plate shows an up-down-up trend, which is consistent with the results of the LAGBs. Theoretically, the GND density in the final microstructure depends on both the transformation strain and the plastic strain degree inherited from the progress of austenitic deformation. This may suggest that the austenite grain undergoes various metallurgical events, i.e. deformation temperature, strain rates, and deformation degree during the hot bending process before phase transformation [33].

4.3 Effect of parent austenite and martensite packet on strength

Figure 13 gives the grain statistics versus bending strain for both CE and OE regions. When the plate was bent to a certain distance like 15 mm (average grain size, CE 12.8 μm and OE 12.9 μm) and 20 mm (average grain size, CE 11.2 μm and OE 11.7 μm), the variation of grain size as a function of straining was less than with the lower bending distance (10 mm (average grain size, CE 21.0 μm and OE 17.6 μm)). For an almost complete DRX condition, the grains slightly coarsened when the bending distance reached 25 mm (average grain size, CE 13.6 μm and OE 12.1 μm). By connecting

it with obtained hardness results, it is not hard to see that the strength of the plate bent at 10 mm is on account of the fact that, as shown below, coarser PA grain with a lower incidence of PA grain boundaries occupies higher hardenability, resulting in the bigger volume fractions of martensite in the final product phases and thereby higher hardness [45].

To gain further insight into detailed characteristics of final microstructures, it has been primarily proposed that a parent austenite grain is split into several packets [35, 45]. Each unique packet can be classified into a combination of blocks, sub-blocks, and laths. Lath as the basic/finest unit of martensite is independent of each other identifying by low-angle boundaries ($> 10.53^\circ$) [35]. During the progress of austenite reconstruction, the packet distributions of each bent plate on both regions (see Fig. 14) were well predicted by the MTEX technique, as well. It can be seen that the packet size shows little deviation in both CE and OE of the specimens bent at 10 and 15 mm (Fig. 14a–d). However, it is clearly observed based on the legend bar that the packet shows a larger size overall from CE than that of OE when the bending distance improved to 20 and 25 mm (Figs. 14e–h). It is worth mentioning that the significant influence of LM structure on the strength and toughness of metal materials,

i.e. low-carbon steels [35] and Fe–C alloys [36] due to the different block and packet sizes. Investigating the evolution of crystallographic and morphological characteristics of martensite in this steel is of great importance to explain the hardness transition on different bent regions in the same specimen. In addition to the effects of SNL, dislocation or DRX given above, another dominant factor that would bring a difference in strength is martensite packet size. The size of the martensite variant and the size of the packet in which the variant is located have a more close impact on the mechanical properties of the material, which has been proposed that the packet size affects the toughness of the martensitic steels [59, 60], and the decreased packet size would increase the strength of steels with LM structure [35]. Thus, it can be speculated that the large gradients of hardness on CE and OE of the specimens bent at 20 and 25 mm was also resulted from the difference in overall packet size.

5 Conclusions

In the current study, the effects of bending degrees on high-strength quenched and micro-alloyed steel during an austenitising bending process were comprehensively investigated. The major conclusions can be drawn below:

- The high consistency between experimental and simulation results is instructive for the practical forming process of railway spring fasteners.
- Both the mean hardness and forming force in the bent region gradually decreased with the increase of bending degree. The high-temperature DRV is mainly responsible for the work hardening process due to the dislocation accumulation. Combining the results of LAGBs and HAGBs, it can be speculated that the DRX was completed after 20 mm but before 25 mm of the bending distances. Thus, the DRV played a major role after 20-mm bending distance as the result of scond rise in LAGBs and GNDs.
- SNL as another essential factor clarifies the smaller hardness nearby the central line throughout the plate thickness, which tends to move to the outer surface during straining.
- Through austenite reconstruction, the coarser PA grains with a lower incidence of PA grain boundaries occupy hardenability leading to the bigger volume fractions of martensite in the final product phases and thereby higher hardness. Besides, the overall smaller martensite packet size observed on the outer surfaces of specimens at a larger bending degree explains the higher hardness from another aspect.

Acknowledgements The authors are so grateful for the financial support from the Australian Research Council (ARC) ITTC-Rail Centre at the University of Wollongong (UOW). The authors are thankful for the support of our industrial partner: the Innovative Technology Beijing Company. We finally wish to thank Azdiar A. Gazder for his contributions to the parent reconstruction, who is the microscopy expert from EMC of UOW.

Author contribution Yao Lu: Methodology, data curation, writing original draft. Haibo Xie: Review and editing. Jun Wang: Methodology, review and editing. Fanghui Jia: Software. Fei Lin: Formal analysis. Cunlong Zhou: Investigation. Jianzhong Xu: Resources. Jingtao Han: Conceptualization, supervision, methodology. Zhengyi Jiang: Supervision, review and editing, project administration.

Funding Open Access funding enabled and organized by CAUL and its Member Institutions.

Data availability All data included in the current work are available upon request by contacting the corresponding author.

Declarations

Ethics approval The author obliged all the rules regarding the ethics in publication.

Consent to participate All the authors consent regarding the data provided in the text as well as the order of authorship.

Consent for publication All the authors are consent regarding publication immediately after acceptance.

Competing interests The authors declare no competing interests.

Open Access This article is licensed under a Creative Commons Attribution 4.0 International License, which permits use, sharing, adaptation, distribution and reproduction in any medium or format, as long as you give appropriate credit to the original author(s) and the source, provide a link to the Creative Commons licence, and indicate if changes were made. The images or other third party material in this article are included in the article's Creative Commons licence, unless indicated otherwise in a credit line to the material. If material is not included in the article's Creative Commons licence and your intended use is not permitted by statutory regulation or exceeds the permitted use, you will need to obtain permission directly from the copyright holder. To view a copy of this licence, visit <http://creativecommons.org/licenses/by/4.0/>.

References

1. Lu Y, Xie H, Wang J, Li Z, Jia F, Wu H, Han J, Jiang Z (2020) Influence of hot compressive parameters on flow behaviour and microstructure evolution in a commercial medium carbon micro-alloyed spring steel. *J Manuf Process* 58:1171–1181. <https://doi.org/10.1016/j.jmapro.2020.09.021>
2. Hasap A, Paitekul P, Noraphaiphapaksa N, Kanchanomai C (2018) Analysis of the fatigue performance of elastic rail clip. *Eng Fail Anal* 92:195–204. <https://doi.org/10.1016/j.engfailanal.2018.05.013>
3. Lakusic S, Bartos D, Ante Goran B (2005) Experimental and numerical analysis of the rail fastening spring clips types SKL11-SKL12, Symposium on experimental methods in Solid Mechanics. 22nd DANUBIA-ADRIA Symposium on Experimental Methods

- in Solid Mechanics, Parma, University of Parma, 2005, pp. 248–249
4. Ling L, Li W, Shang H, Xiao X, Wen Z, Jin X (2014) Experimental and numerical investigation of the effect of rail corrugation on the behaviour of rail fastenings. *Veh Syst Dyn* 52:1211–1231. <https://doi.org/10.1080/00423114.2014.934844>
 5. Mohammadzadeh S, Ahadi S, Nouri M (2014) Stress-based fatigue reliability analysis of the rail fastening spring clip under traffic loads. *Latin Am J Solids Struc* 11:993–1011
 6. Yuan Z, Zhu S, Yuan X, Zhai W (2021) Vibration-based damage detection of rail fastener clip using convolutional neural network: experiment and simulation. *Eng Fail Anal* 119:104906. <https://doi.org/10.1016/j.engfailanal.2020.104906>
 7. Ardehali Barani A, Ponge D, Raabe D (2006) Refinement of grain boundary carbides in a Si–Cr spring steel by thermomechanical treatment. *Mater Sci Eng A* 426:194–201. <https://doi.org/10.1016/j.msea.2006.04.002>
 8. Hase K, Garcia-Mateo C, Bhadeshia HKDH (2006) Bimodal size-distribution of bainite plates. *Mater Sci Eng A* 438–440:145–148. <https://doi.org/10.1016/j.msea.2005.12.070>
 9. Saha Podder A, Bhadeshia HKDH (2010) Thermal stability of austenite retained in bainitic steels. *Mater Sci Eng A* 527:2121–2128. <https://doi.org/10.1016/j.msea.2009.11.063>
 10. Yin B, Han Y, Wang W, Li H, Liu Y, Ran X (2019) Flow characteristics of a medium–high carbon Mn–Si–Cr alloyed steel at high temperatures. *J Mater Eng Perform* 28:5104–5115. <https://doi.org/10.1007/s11665-019-04197-7>
 11. Hu F, Hodgson PD, Wu KM (2014) Acceleration of the super bainite transformation through a coarse austenite grain size. *Mater Lett* 122:240–243. <https://doi.org/10.1016/j.matlet.2014.02.051>
 12. Garcia-Mateo C, Caballero FG, Bhadeshia HKDH (2003) Development of Hard Bainite. *ISIJ Int* 43:1238–1243. <https://doi.org/10.2355/isijinternational.43.1238>
 13. Lu Y, Xie H, Wang J, Li Z, Lin F, Han J, Han J, Jiang Z (2021) Characteristic flow behaviour prediction and microstructure analysis of a commercial Si–Cr micro-alloyed spring steel under isothermal compression. *Vacuum* 186:110066. <https://doi.org/10.1016/j.vacuum.2021.110066>
 14. Xu G, Liu F, Wang L, Hu H (2013) A new approach to quantitative analysis of bainitic transformation in a superbainite steel. *Scr Mater* 68:833–836. <https://doi.org/10.1016/j.scriptamat.2013.01.033>
 15. Zhang MX, Kelly PM (2006) Crystallography of carbide-free bainite in a hard bainitic steel. *Mater Sci Eng A* 438–440:272–275. <https://doi.org/10.1016/j.msea.2006.05.022>
 16. Morales-Rivas L, Yen H-W, Huang B-M, Kuntz M, Caballero FG, Yang J-R, Garcia-Mateo C (2015) Tensile response of two nanoscale bainite composite-like structures. *JOM* 67:2223–2235. <https://doi.org/10.1007/s11837-015-1562-x>
 17. Zhou Q, Qian L, Meng J, Zhao L, Zhang F (2015) Low-cycle fatigue behavior and microstructural evolution in a low-carbon carbide-free bainitic steel. *Mater Des* 85:487–496. <https://doi.org/10.1016/j.matdes.2015.06.172>
 18. Morales-Rivas L, Garcia-Mateo C, Kuntz M, Sourmail T, Caballero FG (2016) Induced martensitic transformation during tensile test in nanostructured bainitic steels. *Mater Sci Eng A* 662:169–177. <https://doi.org/10.1016/j.msea.2016.03.070>
 19. Wang Z, Liu X, Xie F, Lai C, Li H, Zhang Q (2018) Dynamic recrystallization behavior and critical strain of 51CrV4 high-strength spring steel during hot deformation. *JOM* 70:2385–2391. <https://doi.org/10.1007/s11837-018-3054-2>
 20. Han Y, Yan S, Yin B, Li H, Ran X (2018) Effects of temperature and strain rate on the dynamic recrystallization of a medium-high-carbon high-silicon bainitic steel during hot deformation. *Vacuum* 148:78–87. <https://doi.org/10.1016/j.vacuum.2017.11.007>
 21. Huang Y-M (2007) Finite element analysis on the V-die coining bend process of steel metal. *The International J Adv Manuf Technol* 34:287–294. <https://doi.org/10.1007/s00170-007-1054-4>
 22. Mandal A, Syed B, Bhandari KK, Bhattacharya B, Deb A, Singh SB, Chakrabarti D (2019) Cold-bending of linepipe steel plate to pipe, detrimental or beneficial?. *Mater Sci Eng A* 746:58–72. <https://doi.org/10.1016/j.msea.2019.01.005>
 23. Khan SH, Saeed Ahmed M, Ali F, Nusair A, Iqbal MA (2009) Investigation of high strength steel bending. *Eng Fail Anal* 16:128–135. <https://doi.org/10.1016/j.engfailanal.2008.01.002>
 24. Lawanwong K, Hamasaki H, Hino R, Yoshida F (2020) Double-action bending for eliminating springback in hat-shaped bending of advanced high-strength steel sheet. *The Int J Adv Manuf Technol* 106:1855–1867. <https://doi.org/10.1007/s00170-019-04678-y>
 25. Poulin CM, Korkolis YP, Kinsey BL, Knezevic M (2019) Over five-times improved elongation-to-fracture of dual-phase 1180 steel by continuous-bending-under-tension. *Mater Des* 161:95–105. <https://doi.org/10.1016/j.matdes.2018.11.022>
 26. Liu Y, Fan D, Bhat SP, Srivastava A (2020) Ductile fracture of dual-phase steel sheets under bending. *Int J Plastic* 125:80–96. <https://doi.org/10.1016/j.ijplas.2019.08.019>
 27. Chung KH, Lee W, Kim JH, Kim C, Park SH, Kwon D, Chung K (2009) Characterization of mechanical properties by indentation tests and FE analysis – validation by application to a weld zone of DP590 steel. *Int J Solids Struc* 46:344–363. <https://doi.org/10.1016/j.ijsolstr.2008.08.041>
 28. Barrett TJ, Knezevic M (2020) Modeling material behavior during continuous bending under tension for inferring the post-necking strain hardening response of ductile sheet metals: Application to DP 780 steel. *Int J Mech Sci* 174:105508. <https://doi.org/10.1016/j.ijmecsci.2020.105508>
 29. Simonett E, Ghiotti A, Bruschi S (2021) High accuracy direct hot bending of hollow profiles. *Manufac Lett* 27:63–66. <https://doi.org/10.1016/j.mfglet.2020.12.005>
 30. Niessen F, Nyssönen T, Gazder AA, Hielscher RJAPA (2021) Parent grain reconstruction from partially or fully transformed microstructures in MTEX
 31. Yanagida A, Azushima A (2009) Evaluation of coefficients of friction in hot stamping by hot flat drawing test. *CIRP Annals* 58:247–250. <https://doi.org/10.1016/j.cirp.2009.03.091>
 32. Li Z, Zhao J, Jia F, Zhang Q, Liang X, Jiao S, Jiang Z (2019) Numerical and experimental investigation on the forming behaviour of stainless/carbon steel bimetal composite. *The Int J Adv Manuf Technol* 101:1075–1083. <https://doi.org/10.1007/s00170-018-2985-7>
 33. Lan L, Zhou W, Misra RDK (2019) Effect of hot deformation parameters on flow stress and microstructure in a low carbon microalloyed steel. *Mater Sci Eng A* 756:18–26. <https://doi.org/10.1016/j.msea.2019.04.039>
 34. Sohn SS, Han SY, Shin SY, Bae J-H, Lee S (2013) Analysis and estimation of the yield strength of API X70 and X80 linepipe steels by double-cycle simulation tests. *Met Mater Int* 19:377–388. <https://doi.org/10.1007/s12540-013-3002-1>
 35. Kitahara H, Ueji R, Tsuji N, Minamino Y (2006) Crystallographic features of lath martensite in low-carbon steel. *Acta Mater* 54:1279–1288. <https://doi.org/10.1016/j.actamat.2005.11.001>
 36. Morito S, Tanaka H, Konishi R, Furuhashi T, Maki T (2003) The morphology and crystallography of lath martensite in Fe–C alloys. *Acta Mater* 51:1789–1799. [https://doi.org/10.1016/S1359-6454\(02\)00577-3](https://doi.org/10.1016/S1359-6454(02)00577-3)
 37. Lan L, Yu M, Qiu C (2019) On the local mechanical properties of isothermally transformed bainite in low carbon steel. *Mater Sci Eng A* 742:442–450. <https://doi.org/10.1016/j.msea.2018.11.011>
 38. Flower HM, Lindley TC (2000) Electron backscattering diffraction study of acicular ferrite, bainite, and martensite steel

- microstructures. *Mater Sci Technol* 16:26–40. <https://doi.org/10.1179/026708300773002636>
39. Sun H, Sun Y, Zhang R, Wang M, Tang R, Zhou Z (2014) Hot deformation behavior and microstructural evolution of a modified 310 austenitic steel. *Mater Des* 64:374–380. <https://doi.org/10.1016/j.matdes.2014.08.001>
 40. Sun L, Muszka K, Wynne BP, Palmiere EJ (2014) Effect of strain path on dynamic strain-induced transformation in a microalloyed steel. *Acta Mater* 66:132–149. <https://doi.org/10.1016/j.actamat.2013.11.062>
 41. Han Y, Liu G, Zou D, Liu R, Qiao G (2013) Deformation behavior and microstructural evolution of as-cast 904L austenitic stainless steel during hot compression. *Mater Sci Eng A* 565:342–350. <https://doi.org/10.1016/j.msea.2012.12.043>
 42. Kim YM, Lee H, Kim NJ (2008) Transformation behavior and microstructural characteristics of acicular ferrite in linepipe steels. *Mater Sci Eng A* 478:361–370. <https://doi.org/10.1016/j.msea.2007.06.035>
 43. Liu J, Chang H, Wu R, Hsu TY, Ruan X (2000) Investigation on hot deformation behavior of AISI T1 high-speed steel. *Mater Charact* 45:175–186. [https://doi.org/10.1016/S1044-5803\(00\)00071-1](https://doi.org/10.1016/S1044-5803(00)00071-1)
 44. Lu Y, Xie H, Wang J, Jia F, Li Z, Lin F, Pan D, Han J, Jiang Z (2021) Simulation, microstructure and austenite reconstruction of a medium carbon micro-alloyed steel subjected to an austenitising bending process. *Mater Lett* 130772. <https://doi.org/10.1016/j.matlet.2021.130772>
 45. Javaheri V, Kolli S, Grande B, Porter D (2019) Insight into the induction hardening behavior of a new 0.40% C microalloyed steel: Effects of initial microstructure and thermal cycles. *Mater Charact* 149:165–183. <https://doi.org/10.1016/j.matchar.2019.01.029>
 46. Hidalgo J, Santofimia MJ (2016) Effect of Prior Austenite Grain Size Refinement by Thermal Cycling on the Microstructural Features of As-Quenched Lath Martensite. *Metall and Mater Trans A* 47:5288–5301. <https://doi.org/10.1007/s11661-016-3525-4>
 47. Peng F, Xu Y, Li J, Gu X, Wang X (2019) Interaction of martensite and bainite transformations and its dependence on quenching temperature in intercritical quenching and partitioning steels. *Mater Des* 181:107921. <https://doi.org/10.1016/j.matdes.2019.107921>
 48. Kundu S, Verma AK, Sharma V (2012) Quantitative Analysis of Variant Selection for Displacive Transformations Under Stress. *Metall and Mater Trans A* 43:2552–2565. <https://doi.org/10.1007/s11661-011-0971-x>
 49. Thipprakmas S (2010) Finite element analysis of punch height effect on V-bending angle. *Mater Des* 31:1593–1598. <https://doi.org/10.1016/j.matdes.2009.09.019>
 50. Li H, Ma J, Liu BY, Gu RJ, Li GJ (2018) An insight into neutral layer shifting in tube bending. *Int J Mach Tools Manuf* 126:51–70. <https://doi.org/10.1016/j.ijmactools.2017.11.013>
 51. Li FF, Fang G (2020) Modeling of 3D plastic anisotropy and asymmetry of extruded magnesium alloy and its applications in three-point bending. *Int J Plastic* 130:102704. <https://doi.org/10.1016/j.ijplas.2020.102704>
 52. Ma L, Ma Z, Jia W, Lv Y, Jiang Y, Xu H, Liu P (2015) Research and verification on neutral layer offset of bar in two-roll straightening process. *The Int J Adv Manuf Technol* 79:1519–1529. <https://doi.org/10.1007/s00170-015-6899-3>
 53. Kim DW, Sohn SS, Kim W-K, Kim K-S, Lee S (2018) Study of Bauschinger effect of acicular ferrite and polygonal ferrite through ex-situ interrupted bending tests in API X80 linepipe steels. *Sci Rep* 8:15598. <https://doi.org/10.1038/s41598-018-34046-x>
 54. Ramazani A, Mukherjee K, Schwedt A, Goravanchi P, Prahl U, Bleck W (2013) Quantification of the effect of transformation-induced geometrically necessary dislocations on the flow-curve modelling of dual-phase steels. *Int J Plastic* 43:128–152. <https://doi.org/10.1016/j.ijplas.2012.11.003>
 55. Li Z, Zhao J, Jia F, Lu Y, Liang X, Yuan X, Jiao S, Zhou C, Jiang Z (2020) Hot deformation behaviour and interfacial characteristics of bimetal composite at elevated temperatures. *Intermetallics* 125:106893. <https://doi.org/10.1016/j.intermet.2020.106893>
 56. Ma X, Huang C, Moering J, Ruppert M, Höppel HW, Göken M, Narayan J, Zhu Y (2016) Mechanical properties of copper/bronze laminates: Role of interfaces. *Acta Mater* 116:43–52. <https://doi.org/10.1016/j.actamat.2016.06.023>
 57. Jiang J, Britton TB, Wilkinson AJ (2013) Evolution of dislocation density distributions in copper during tensile deformation. *Acta Mater* 61:7227–7239. <https://doi.org/10.1016/j.actamat.2013.08.027>
 58. Bay B, Hansen N, Hughes DA, Kuhlmann-Wilsdorf D (1992) Overview no. 96 evolution of f.c.c. deformation structures in polyslip. *Acta Metall Mater* 40:205–219. [https://doi.org/10.1016/0956-7151\(92\)90296-Q](https://doi.org/10.1016/0956-7151(92)90296-Q)
 59. Swarr T, Krauss G (1976) The effect of structure on the deformation of as-quenched and tempered martensite in an Fe-0.2 pct C alloy. *Metall Trans A* 7:41–48. <https://doi.org/10.1007/BF02644037>
 60. Lu Y, Xie H, Wang J, Jia F, Li Z, Kamali H, Xu J, Han J, Jiang Z (2022) Design of a novel austenitising bending process in forming characteristics of highstrength quenched and micro-alloyed steel: Experiment and simulation. *Mater Des* 215:110458. <https://doi.org/10.1016/j.matdes.2022.110458>

Publisher's Note Springer Nature remains neutral with regard to jurisdictional claims in published maps and institutional affiliations.

2022-05-11

Ex situ analysis of high-strength quenched and micro-alloyed steel during austenitising bending process: numerical simulation and experimental investigation

Lu, Yao

Springer

Lu Y, Xie H, Wang J, et al., (2022) Ex situ analysis of high-strength quenched and micro-alloyed steel during austenitising bending process: numerical simulation and experimental investigation, *The International Journal of Advanced Manufacturing Technology*, Volume 120, Issue 11-12, pp. 8293-8309

<https://doi.org/10.1007/s00170-022-09261-6>

Downloaded from Cranfield Library Services E-Repository